

# Zodiacal exoplanets in time – XI. The orbit and radiation environment of the young M dwarf-hosted planet K2-25b

E. Gaidos<sup>1</sup>,<sup>1</sup>★ T. Hirano,<sup>2</sup> D. J. Wilson<sup>3</sup>,<sup>3</sup> K. France,<sup>4</sup> K. Rockcliffe,<sup>5</sup> E. Newton,<sup>5</sup> G. Feiden<sup>6</sup>,<sup>6</sup> V. Krishnamurthy<sup>7</sup>,<sup>7</sup> H. Harakawa,<sup>7,8</sup> K. W. Hodapp,<sup>9</sup> M. Ishizuka,<sup>10</sup> S. Jacobson,<sup>9</sup> M. Konishi,<sup>11</sup> T. Kotani,<sup>8,12,13</sup> T. Kudo,<sup>7,8</sup> T. Kurokawa,<sup>8,14</sup> M. Kuzuhara,<sup>8,12</sup> J. Nishikawa,<sup>8,12,13</sup> M. Omiya,<sup>8,12</sup> T. Serizawa,<sup>14</sup> M. Tamura,<sup>8,10,12</sup> A. Ueda<sup>12</sup> and S. Vievard<sup>7,8</sup>

<sup>1</sup>Department of Earth Sciences, University of Hawai‘i at Mānoa, Honolulu, HI 96822, USA

<sup>2</sup>Department of Earth and Planetary Sciences, Tokyo Institute of Technology, 2-12-1 Ookayama, Meguro-ku, Tokyo 152-8551, Japan

<sup>3</sup>McDonald Observatory, University of Texas at Austin, Austin, TX 78712, USA

<sup>4</sup>Laboratory for Atmospheric and Space Physics, University of Colorado, Boulder, CO 80309, USA

<sup>5</sup>Department of Physics and Astronomy, Dartmouth College, Hanover, NH 03755, USA

<sup>6</sup>Department of Physics and Astronomy, University of North Georgia, Dahlonega, GA 30597, USA

<sup>7</sup>Subaru Telescope, 650 N. Aohoku Place, Hilo, HI 96720, USA

<sup>8</sup>Astrobiology Center, NINS, 2-21-1 Osawa, Mitaka, Tokyo 181-8588, Japan

<sup>9</sup>Institute for Astronomy, University of Hawai‘i, 640 N. Aohoku Place, Hilo, HI 96720, USA

<sup>10</sup>Department of Astronomy, Graduate School of Science, The University of Tokyo, 7-3-1 Hongo, Bunkyo-ku, Tokyo 113-0033, Japan

<sup>11</sup>Faculty of Science and Technology, Oita University, 700 Dannoharu, Oita 870-1192, Japan

<sup>12</sup>National Astronomical Observatory of Japan, NINS, 2-21-1 Osawa, Mitaka, Tokyo 181-8588, Japan

<sup>13</sup>Department of Astronomy, School of Science, The Graduate University for Advanced Studies (SOKENDAI), 2-21-1 Osawa, Mitaka, Tokyo 181-8588, Japan

<sup>14</sup>Institute of Engineering, Tokyo University of Agriculture and Technology, 2-24-16, Nakacho, Koganei, Tokyo 184-8588, Japan

Accepted 2020 August 3. Received 2020 July 13; in original form 2020 June 22

## ABSTRACT

M dwarf stars are high-priority targets for searches for Earth-size and potentially Earth-like planets, but their planetary systems may form and evolve in very different circumstellar environments than those of solar-type stars. To explore the evolution of these systems, we obtained transit spectroscopy and photometry of the Neptune-size planet orbiting the  $\approx 650$ -Myr-old Hyades M dwarf K2-25. An analysis of the variation in spectral line shape induced by the Doppler ‘shadow’ of the planet indicates that the planet’s orbit is closely aligned with the stellar equator ( $\lambda = -1.7^{+5.8}_{-3.7}$  deg), and that an eccentric orbit found by previous work could arise from perturbations by another planet on a coplanar orbit. We detect no significant variation in the depth of the He I line at 1083 nm during transit. A model of atmospheric escape as an isothermal Parker wind with a solar composition shows that this non-detection is not constraining compared to escape rate predictions of  $\sim 0.1 M_{\oplus} \text{ Gyr}^{-1}$ ; at such rates, at least several Gyr are required for a Neptune-like planet to evolve into a rocky super-Earth.

**Key words:** techniques: spectroscopic – Sun: UV radiation – planets and satellites: atmospheres – planets and satellites: physical evolution – stars: activity – planetary systems.

## 1 INTRODUCTION

M dwarfs are numerous hydrogen-burning stars with comparatively low masses, small radii, and low luminosities that promote the detection of Earth-size and potentially Earth-like planets in compact circumstellar habitable zones. However, the formation and environments of planets on short-period orbits around these stars could differ substantially from those of true Earth analogues. M dwarfs more frequently host compact multiplanet systems (Muirhead et al. 2015) and host more close-in planets (Mulders, Pascucci & Apai 2015), possibly a consequence of differences in the structure and evolution of their circumstellar discs (Kastner et al. 2016; Gaidos 2017). M

dwarfs have elevated X-ray and UV emission (XUV) relative to their bolometric (total) luminosities, and exhibit a different evolution in the rotation and magnetic activity responsible for this emission (Matt et al. 2015). M dwarf stars have prolonged pre-main-sequence phases compared to their solar-mass counterparts. Such differences could drive planets and their atmospheres on divergent evolutionary pathways as a result of the runaway greenhouse effect (Luger & Barnes 2015), photodissociation of molecules (Tian et al. 2014), and escape of primordial H/He atmospheres to space (Owen 2019).

The evolution of planets can be investigated by observations of systems in nearby young stellar clusters and comoving groups. For transiting planets, it is possible to make unambiguous radius and mass estimates to determine bulk density and constrain composition, to measure the atmosphere via transmission spectroscopy, and to constrain the orbit via measurements of the duration and times

\* E-mail: gaidos@hawaii.edu

of transit as well as the spin–orbit obliquity via the Rossiter–McLaughlin effect (Triaud 2017).

2MASS J04130560+1514520 is a member of the  $\approx 650$ -Myr-old Hyades cluster that hosts a Neptune-size planet on a 3.45-d transiting orbit. The planet was discovered in *K2* data (Mann et al. 2016) and designated K2-25b. Along with the K2-126 system (Mann et al. 2018), it stands because of its young age and proximity ( $\approx 50$  pc). Thao et al. (2020) compared the transit depth as measured with *Spitzer* 4.5  $\mu\text{m}$  observations to that measured with *K2* data ( $\sim 0.8 \mu\text{m}$ ) to rule out a solar-composition, H-rich atmosphere. Precise measurement of the transit duration, combined with a *Gaia*-improved estimates of stellar properties estimation, indicates an orbital eccentricity  $e > 0.2$ , suggestive of perturbation by a companion planet or star. An interaction like the Kozai–Lidov resonance would also have left the planet on a highly inclined orbit. The host star is rapidly rotating (1.88-d period) and has significant rotational variability indicative of star-spots, and thus magnetic activity. K2-25b’s proximity to the star (0.035 au) thus makes its atmosphere vulnerable to XUV-driven escape.

To further constrain the orbit and search for atmospheric escape from K2-25b, we made spectroscopic and photometric observations of a transit on UT 2019 October 13 to obtain information on the change in line shape due to the Rossiter–McLaughlin effect (‘Doppler tomography’) and absorption in the 1083 nm line of metastable ‘triplet’ (*ortho*) He I (Oklopčić & Hirata 2018). We also use *Hubble Space Telescope* (*HST*) observations of an earlier transit (Rockcliffe et al., in preparation) to constrain the UV emission from the star.

## 2 OBSERVATIONS AND DATA REDUCTION

### 2.1 Infrared spectroscopy

77 spectra of K2-25 were obtained with the IRD infrared echelle spectrograph (Tamura et al. 2012; Kotani et al. 2018) on the Subaru telescope on Maunakea over a 430-d interval beginning 2018 August 17. IRD covers 970–1730 nm with  $\lambda/\Delta\lambda \approx 70\,000$ . 29 spectra were obtained over a 100-min interval, including the 40-min-long transit of K2-25b, on the night of UT 2019 October 13. Four and 15 spectra were obtained during the previous and following nights, respectively. Integration times were 5 min during and near the transit, and 10 min otherwise. Using the *iraf* echelle package (Tody 1986) and custom software, we extracted 1D spectra after flat-fielding and scattered light subtraction. Wavelengths were calibrated using the comparison spectra of the Th–Ar lamp taken during the run. Typical signal-to-noise (S/N) ratios at 1000 nm were 20–25 and 25–35 per pixel for 300- and 600-s integrations, respectively.

### 2.2 Photometry

Continuous imaging of K2-25 was obtained for 14.5 h starting 12 h before transit with the LCOGT 0.4-m telescopes and SBIG CCD detectors at the Tenerife (TFN) and McDonald Observatory (ELP) sites. Each 300-s integration was made through a Sloan *r*’ filter. Images were automatically processed using the *banzai* pipeline (McCully et al. 2018). To remove atmospheric effects, a reference light curve was constructed using a set of 130 stars that were iteratively selected for low variability with respect to an aggregate mean. TFN data are of low photometric quality due to weather and are not presented here.

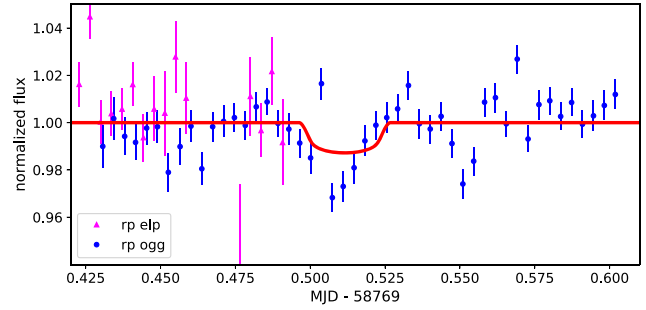


**Figure 1.** Top: *r*-band light curve of K2-25 from LCOGT McDonald (ELP) and Haleakala (OGG) 0.4-m telescopes. The red curve is apytransit model (Parviainen 2015) using the parameters of Thao et al. (2020).

### 2.3 UV spectroscopy

We observed K2-25 with *HST* and the Space Telescope Imaging Spectrometer (STIS; Riley 2017) during visits on 2017 March 23 and October 31. During each visit, eight integrations were obtained with the G140M grating and the far-ultraviolet multi-anode microchannel array (FUV-MAMA) in TIME-TAG mode. Four of the 16 integrations were 1993 s and the remainder were 2054 s, spanning the observable window of the *HST* orbit. These data were reduced using the *calstsis* pipeline. The background, dominated by geocoronal emission at 1215 Å, is negligible for the wavelength range of concern here. The fluxes in the N v doublet (1238.821 and 1242.804 Å) were calculated for each exposure using equation (1) from France et al. (2018). The second visit suffered a large wavelength offset and required a correction of +0.3 Å. Examination of the N v light curves identified one integration potentially contaminated by a flare during each visit and these were excluded from further analysis. The spectral continuum was estimated by calculating the mean flux in 1 Å bins on either side of each line and linearly interpolating. Fluxes between the two visits did not significantly differ and the total N v line flux averaged over the two visits is  $2.8 \pm 0.3 \times 10^{-16} \text{ erg s}^{-1} \text{ cm}^{-2}$ .

## 3 ANALYSIS AND RESULTS

### 3.1 Rossiter–McLaughlin effect and Doppler-shadow analysis

Our LCOGT observations confirm that the transit occurred approximately as predicted by the ephemeris of Thao et al. (2020) (Fig. 1). The transit appears 6 min earlier than predicted ( $\pm 1$  min) and significantly deeper, most likely due to systematics in the photometry. To measure the spin–orbit obliquity, we analysed the mean line profiles in IRD spectra obtained during the transit. Following Hirano et al. (2020b), we computed the cross-correlation function (CCF) between each spectrum and a telluric-free template spectrum of the M4 dwarf GJ 699 (Hirano et al. 2020c). Before computing CCFs, we divided each spectrum by the normalized spectrum of a telluric standard star obtained on the same night. To make a high S/N CCF for K2-25, we combined the normalized CCFs after correcting for the barycentric motion of Earth. This mean ‘out-of-transit’ CCF was then subtracted from individual normalized CCFs to visualize the instantaneous variation of the line profile.

The left-hand panel of Fig. 2 plots the residual CCFs versus time. The loss of the spectral contribution from the part of the stellar disc occulted by the planet should appear as a moving feature (blue band) during the transit (between the horizontal dotted lines), but is

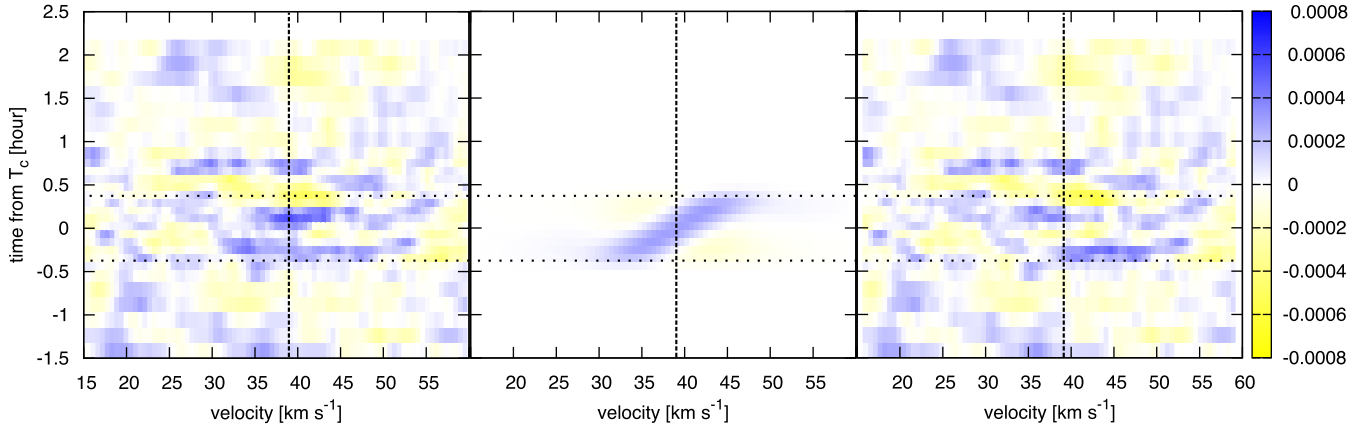


**Figure 2.** Residual CCF maps based on IRD spectra of K2-25 obtained during a transit of ‘b’ on UT 2019 October 13. The left-hand and middle panels are the observed residual CCF and best-fitting model, respectively. The right-hand panel is the residual map after subtracting the best-fitting model. The vertical dashed line marks the centre of the mean CCF ( $\approx 39 \text{ km s}^{-1}$ ) at the systemic radial velocity (RV) of K2-25, and the horizontal dotted lines indicate transit ingress and egress.

not apparent due to low S/N. To estimate the projected obliquity  $\lambda$ , we compared the observed residual CCFs to a model based on mock IRD spectra with different values of the stellar rotation velocity  $v \sin i$  ( $4\text{--}11 \text{ km s}^{-1}$ ) and planet position on the stellar disc (see Hirano et al. 2020b, for more details). We fit these models to the observed residual CCF map with a Markov chain Monte Carlo (MCMC) analysis without a prior on  $v \sin i$ . However, this MCMC fit did not converge in  $v \sin i$ , most likely due to low S/N in the CCF around the transit. We thus imposed a prior on  $v \sin i$  based on the observed mean CCF. A comparison between the observed and model CCFs gave  $v \sin i = 7.71 \pm 0.29 \text{ km s}^{-1}$ , which agrees with that derived by Mann et al. (2016). Using this value as a Gaussian prior, we refit the observed residual CCFs by MCMC. In the analysis, we also allowed the scaled semimajor axis ( $a/R_*$ ), impact parameter  $b$ , and mid-transit time  $T_c$  to vary with Gaussian priors based on the values in Thao et al. (2020).

Our MCMC fit yielded an obliquity of  $\lambda = -1.7^{+5.8}_{-3.7} \text{ deg}$ , consistent with spin–orbit alignment. The middle panel of Fig. 2 shows the best-fitting theoretical model for the observed CCF map. To validate this detection, we confirmed that the depth of the feature is consistent with predictions, Doppler-shifting each residual CCF frame during the transit so that the shifted CCF has the expected peak at the systemic RV in Fig. 2, and averaging the shifted CCFs. The red solid line in the upper panel of Fig. 3 plots the combined residual CCF during the transit; the observed peak height is consistent with that of the combined theoretical CCF derived from the same spectra. For comparison, the blue dashed line in the same panel shows the combined out-of-transit CCFs using the same number of closest frames to the transit. The observed peak height of the combined in-transit CCF is 5–6 times higher than the scatter of the combined out-of-transit CCF ( $\approx 0.000054$ ).

As a further test, we checked if the combined in-transit CCF also has the highest peak near  $\lambda = 0 \text{ deg}$ . To do so, we combined the in-transit residual CCFs, each Doppler-shifted based on a set of  $(\lambda, v \sin i)$  values, and fitted the resulting mean in-transit CCFs by a Gaussian. For each set of  $(\lambda, v \sin i)$  values, we recorded the Gaussian height and generated its contour map. The lower panel of Fig. 3 shows that the highest CCF peak ( $>0.0003$ ) fall in the range  $-21 \lesssim \lambda \lesssim +1 \text{ deg}$ , in agreement with  $\lambda = -1.7^{+5.8}_{-3.7} \text{ deg}$  from the direct MCMC fitting above, while the CCF height has a very weak dependence on  $v \sin i$  within the simulated range.

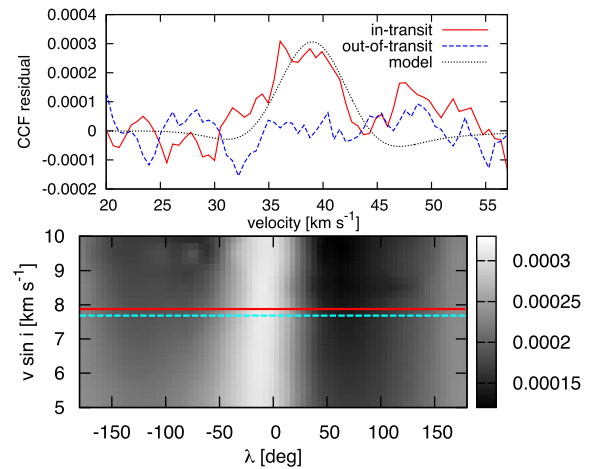


**Figure 3.** Top: Average residual CCFs during (red) and outside (blue) the transit of K2-25b. The same number of spectra were used in each profile. The black dotted line is the best-fitting model. Bottom: Grey-scale map of the peak height of the combined in-transit CCF for different sets of  $\lambda$  and  $v \sin i$ . The solid (red) and dashed (cyan) horizontal lines are the equatorial rotation velocity estimated from  $P_{\text{rot}}$  and  $v \sin i$  from our spectroscopy, respectively.

### 3.2 1083 nm He I line

A prominent telluric OH line interfered with the stronger unresolved doublet (1083.025 and 1083.034 nm) in the stellar line of He I in IRD spectra obtained in 2018 August and 2019 October, including during the transit. The same line interfered with the weaker singlet (1082.909 nm) line in spectra obtained during January–March 2019, and for consistency we excluded those data from further analysis. We estimated non-transit related variability due to rotation and evolution of active regions on the star using the weaker line. Because the SNR of individual measurements is limited, we determined a best-fitting Voigt profile based on a sum of all spectra shifted into the rest frame of the star. This profile was then fit to individual spectra to estimate the equivalent width (EW). We equated the measurement uncertainty with the intra-night variability ( $20 \text{ mÅ}$ .) Assuming Gaussian-distributed errors, the mean in the 2018 and 2019 intervals are  $63 \pm 4$  and  $100 \pm 4 \text{ mÅ}$ ; the difference indicates long-term variation in the stellar line.

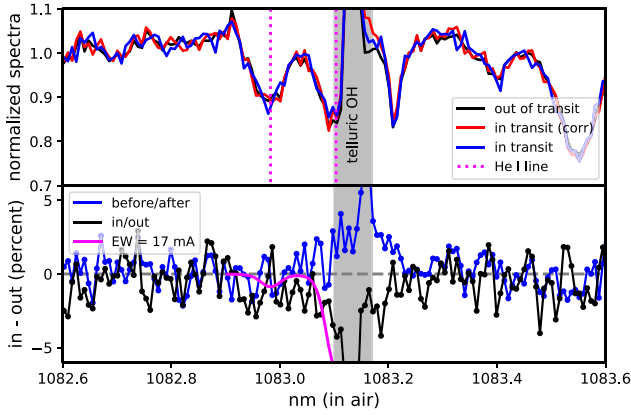


**Figure 4.** Top: Spectra of K2-25 in the vicinity of the He I line inside and outside of the transit of ‘b’. Wavelengths are in air, in the rest frame of the star. The grey zone contains a strong telluric OH line. Bottom: The difference spectrum, compared to a model spectrum of a line with a partial (blueward) EW of 17 mÅ, the 99 per cent confidence detection limit.

To search for an escaping atmosphere, IRD spectra of K2-25 obtained during the transit (eight spectra) and outside transit but on the same night (21 spectra) were coadded. The two combined spectra are shown in the top panel of Fig. 4, and the difference spectrum (in/out minus one) is plotted in the bottom panel, along with the difference between spectra obtained before and after the transit as a comparison. No transit-associated absorption is apparent. We calculated a  $\chi^2$  between the in/out difference spectrum and a Voigt profile of the line assuming a gas temperature of 10 000 K (see below), and established a 99 per cent confidence limit of 17 mÅ on the transit-associated EW over a wavelength range covering the weak singlet line and the uncontaminated blue half of the doublet; this limit is represented by the magenta line in the bottom panel of Fig. 4. We also examined the Paschen  $\beta$  line at 1.282  $\mu\text{m}$ , an important indicator of accretion around young stellar objects (e.g. Yasui et al. 2019) in the same fashion, but we saw no significant difference between the spectra inside and outside of transit.

We converted this EW limit into a limit on atmospheric escape using a model of a spherical, isothermal Parker wind with a solar-like composition (H/He = 10.5) and photochemistry as described in Oklopčić & Hirata (2018) and Gaidos et al. (2020). Densities in such winds are low and the metastable triplet ( $2^3\text{S}$ ) state of the He I transition is primarily populated by recombination of He ionized by extreme-ultraviolet (EUV) photons with energies  $>26.4$  eV ( $\lambda < 504$  Å) and primarily depopulated by ionizing near-ultraviolet (NUV) photons with energies  $>4.8$  eV Å ( $\lambda < 2583$ ; Oklopčić & Hirata 2018). For this reason, interpretation of our observations requires knowledge of the stellar UV irradiation of the planet. Prior to our *HST* observations, no UV spectrum of K2-25 was available, nor was K2-25 detected in either X-rays or UV. To best reproduce both the overall spectral energy distribution of K2-25 and detailed spectral features important to photoionization calculations, we adopted a composite spectrum of the weakly active M3 dwarf GJ 674 produced for the Mega-MUSCLES survey (Froning et al. 2019) and scaled the flux densities in different wavelength ranges to match expected values. The full SED of GJ 674 was created by combining: (a) spectra spanning 1070–5700 Å obtained with nine orbits of observations with *HST* and the Cosmic Origins Spectrograph with the G130M and G230L gratings and STIS with the G140M,

**Table 1.** Irradiation of K2-25b.

Regime	$\lambda\lambda$	Flux at K2-25b	Source
	Å	$10^3 \text{ erg s}^{-1} \text{ cm}^{-2}$	TW = This Work
bolom.	–	$8900 \pm 300$	Thao et al. (2020)
NUV	1750–2800	$4.4 \pm 1.5$	TW + Ansdell et al. (2015)
FUV	1350–1750	$1.3 \pm 0.6$	TW + Ansdell et al. (2015)
Ly $\alpha$	1180–1250	$5.4 \pm 7.0$	TW + Linsky et al. (2013)
EUV	90–360	$1.6 \pm 0.8$	TW + France et al. (2018)
EUV	360–912	$2.2 \pm 2.1$	Linsky et al. (2014)
X-ray	5–120	$7.9 \pm 3.4$	TW + Wright et al. (2018)

G140L, G230L, and G430L gratings; (b) X-ray spectra obtained with  $a \approx 15$  ksec *XMM-Newton* integration; and (c) BT-Settl PHOENIX stellar photosphere models (Allard, Homeier & Freytag 2012). EUV flux densities were estimated using the solar active region scaling relations of Linsky, Fontenla & France (2014). The Ly  $\alpha$  line profile was reconstructed from the STIS G140M spectra via the techniques detailed in Youngblood et al. (2016).

We adjusted the GJ 674 spectrum using estimates of the high-energy emission from K2-25 based partly on its rotation and partly on our *HST* observations of FUV line emission (Section 2). We used an activity–rotation relation formulated in terms of the Rossby number  $Ro = P_{\text{ROT}}/\tau$ , where  $P_{\text{ROT}}$  is the rotation period (1.88 d) and the convective turnover time  $\tau$  for the mass ( $0.26 M_{\odot}$ ; Thao et al. 2020), metallicity ([Fe/H] = +0.15), and age (650 Myr; Martín et al. 2018) of K2-25 was estimated using the standard and magnetic Dartmouth stellar evolution models to be 54 and 59 d, respectively (Feiden 2016). This yields  $Ro = 0.032\text{--}0.035$ , placing it on the ‘saturated’ part of the rotation–activity relation with an expected  $\log L_x/L_{\text{bol}} = -3.05 \pm 0.18$  (Wright et al. 2018). The corresponding luminosities for ‘saturated’ stars in the *GALEX* far-ultraviolet (FUV; 1350–1750 Å) and NUV (1750–2800 Å) channels are about  $3 \times 10^{28}$  and  $9 \times 10^{28} \text{ erg s}^{-1}$ , respectively (Ansdell et al. 2015). We estimated the emission in the Ly  $\alpha$  line using the relation with X-rays of Linsky, France & Ayres (2013). We estimated the EUV emission in the 90–360 Å range using the flux in the Nv line estimated in Section 2 and the FUV–EUV relations described by France et al. (2018). Lastly, we estimated fluxes at 360–912 Å in 40 or 100 Å intervals using the Ly  $\alpha$  flux estimated above and the relations of Linsky et al. (2014). Table 1 lists the estimated irradiance of K2-25b in the different wavelength regimes, using the stellar parameters of Thao et al. (2020).

Densities of neutral and ionized H, singlet and triplet neutral He, ionized He, and electrons are tracked. Line profiles are calculated by integrating from the projected radius of the planet to the Roche radius, accounting for finite optical depth, intrinsic and thermal broadening, and the resolution of the instrument. The mass of K2-25b is not yet determined so we adopted a planet mass  $M_p = 9.7 M_{\oplus}$  based on its radius of  $3.49 R_{\oplus}$  (Thao et al. 2020) and the mass–radius relation of Bashi et al. (2017). Fig. 5 shows the predicted EW of the single line plus the uncontaminated blue half of the doublet as a function of mass-loss rate and wind temperature.

We estimated the energy-limited escape rate by combining the X-ray and photoionizing EUV ( $<912$  Å) irradiances in Table 1 as  $F_{\text{XUV}}$  in (Watson, Donahue & Walker 1981; Erkaev et al. 2007)

$$\dot{M}_{\text{EL}} = \frac{\eta \pi F_{\text{XUV}} R_p^3}{K G M_p}, \quad (1)$$



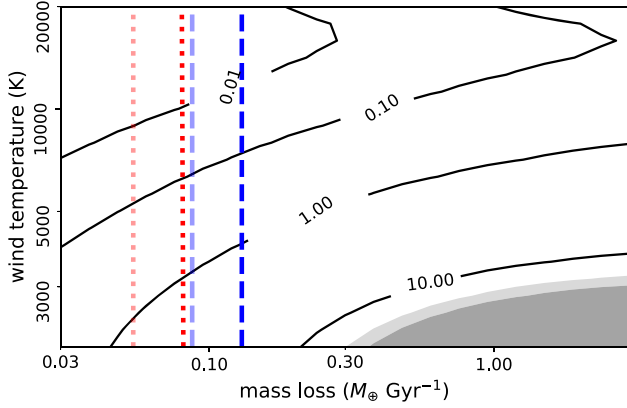


**Figure 5.** Contours of predicted EW (in mÅ) of the 1083 nm triplet He I line versus escape rate in  $M_{\oplus} \text{ Gyr}^{-1}$  ( $\approx 2 \times 10^{12} \text{ g sec}^{-1}$ ) and wind temperature. Only the weak single line and blue half of the doublet are included. The grey zones are excluded at 90 and 99 per cent confidence by upper limits of 14.5 and 17 mÅ. The red dotted and blue dashed lines are predictions using equation (1) and the relations of Kubyskhina et al. (2018), respectively, with the heavy and light version using XUV irradiances with and without the Ly  $\alpha$  contribution, respectively.

where  $\eta \sim 10$  per cent is an efficiency factor (Shematovich, Ionov & Lammer 2014),  $R_{\text{XUV}}$ , the effective radius at the level of the atmosphere where the XUV radiation is absorbed and from which escape occurs (here taken to be  $\approx R_p$ ),  $G$  is the gravitational constant,  $K$  is a correction factor  $\approx 1$  that accounts for a finite Roche radius (Erkaev et al. 2007). We also estimated the escape rate using the empirical relations of Kubyskhina et al. (2018) based on the results of hydrodynamic simulations. Ly  $\alpha$  photons do not ionize H and He but are resonantly scattered by HI and their energy can be absorbed via ionization of, e.g. oxygen (Kockarts 2002). We therefore made separate estimates with and without the Ly  $\alpha$  contribution. These are all of the order of  $0.1 M_{\oplus} \text{ Gyr}^{-1}$  (Fig. 5.) Our model shows that, due to the comparatively low EUV emission from small mid-type *M* type dwarfs such as K2-25, detection of the He I absorption that accompanies expected atmospheric escape rates is challenging (Fig. 5, see also Oklopčić 2019). Since elevated EUV drives both H/He escape and triplet He I production, detection of escape is more practical in younger systems where the central star is more rapidly rotating and magnetically active (e.g. Hirano et al. 2020a).

In summary, we find that the orbit of K2-25b is closely aligned with stellar spin, and the consistency between the  $v \sin i$  derived here and that from the rotation period plus  $R_*$  ( $V_{\text{eq}} = 7.90 \pm 0.26 \text{ km s}^{-1}$ ) means that the stellar inclination is near 90 deg. Stefansson et al. (2020) obtained a similar result using independent observations. This geometry suggests that the orbital eccentricity of K2-25b arose from a perturber in the orbital plane, e.g. an undetected planet on an outer orbit, or that the ratio of obliquity damping to orbit circularization time-scales  $\sim Q'_*/Q'_p (M_*/M_p)^2$  is  $< 1$ , contrary to theoretical expectation (Matsumura, Takeda & Rasio 2008; Li & Winn 2016). Our He I line observations do not usefully constrain atmospheric escape from K2-25b; but at the rates predicted using our estimates of XUV irradiation, the planet could lose  $\sim 5$  per cent by mass of H/He over several few Gyr, enough for a transition from a ‘Neptune’ to a ‘super-Earth’.

## ACKNOWLEDGEMENTS

EG was supported by NASA grant 80NSSC20K0957 (Exoplanets Research Program) and the German Science Foundation (DFG Research Unit FOR2544.) IRD was supported by JSPS KAKENHI grant numbers 19J11805, 19K14783, 18H05442, 15H02063, and 22000005. We made use of the LCOGT network (DDT award 2019B-003, and data obtained by programs 14615 and 15071 of the NASA/ESA *HST* from the archive at STScI, operated by AURA, Inc. (NASA contract NAS 5-26555). We used NASA’s Astrophysics Data System Bibliographic Services, the Centre de Données astronomiques de Strasbourg, NIST’s atomic line data base, *astropy* (Astropy Collaboration 2013), and *scipy* (Virtanen et al. 2019).

## DATA AVAILABILITY

All data are available from the authors or Subaru SMOKA or STScI *HST* archives.

## REFERENCES

- Allard F., Homeier D., Freytag B., 2012, *Phil. Trans. R. Soc. A*, 370, 2765
- Andsell M. et al., 2015, *ApJ*, 798, 41
- Astropy Collaboration, 2013, *A&A*, 558, A33
- Bashi D., Helled R., Zucker S., Mordasini C., 2017, *A&A*, 604, A83
- Erkaev N. V., Kulikov Y. N., Lammer H., Selsis F., Langmayr D., Jaritz G. F., Biernat H. K., 2007, *A&A*, 472, 329
- Feiden G. A., 2016, *A&A*, 593, A99
- France K., Arulanantham N., Fossati L., Lanza A. F., Loyd R. O. P., Redfield S., Schneider P. C., 2018, *ApJS*, 239, 16
- Froning C. S. et al., 2019, *ApJ*, 871, L26
- Gaidos E., 2017, *MNRAS*, 470, L1
- Gaidos E. et al., 2020, *MNRAS*, 495, 650
- Hirano T. et al., 2020a, *ApJ*, 899, L13
- Hirano T. et al., 2020b, *ApJ*, 890, L27
- Hirano T. et al., 2020c, *PASJ*, preprint (arXiv:2007.11013)
- Kastner J. H., Principe D. A., Punzi K., Stelzer B., Gorti U., Pascucci I., Argiroffi C., 2016, *AJ*, 152, 3
- Kockarts G., 2002, *Ann. Geophys.*, 20, 585
- Kotani T. et al., 2018, in Evans C. J., Simard L., Takami H., eds *SPIE Conf. Ser.* Vol. 10702, Ground-Based and Airborne Instrumentation for Astronomy VII. SPIE, Bellingham, p. 1070211
- Kubyskhina D. et al., 2018, *ApJ*, 866, L18
- Li G., Winn J. N., 2016, *ApJ*, 818, 5
- Linsky J. L., France K., Ayres T., 2013, *ApJ*, 766, 69
- Linsky J. L., Fontenla J., France K., 2014, *ApJ*, 780, 61
- Luger R., Barnes R., 2015, *Astrobiology*, 15, 119
- McCully C. et al., 2018, LCOGT/BANZAI: Initial Release. Available at: <http://doi.org/10.5281/zenodo.1257560>
- Mann A. W. et al., 2016, *ApJ*, 818, 46
- Mann A. W. et al., 2018, *AJ*, 155, 4
- Martín E. L., Lodieu N., Pavlenko Y., Béjar V. J. S., 2018, *ApJ*, 856, 40
- Matsumura S., Takeda G., Rasio F. A., 2008, *ApJ*, 686, L29
- Matt S. P., Brun A. S., Baraffe I., Bouvier J., Chabrier G., 2015, *ApJ*, 799, L23
- Muirhead P. S. et al., 2015, *ApJ*, 801, 18
- Mulders G. D., Pascucci I., Apai D., 2015, *ApJ*, 798, 112
- Oklopčić A., 2019, *ApJ*, 881, 133
- Oklopčić A., Hirata C. M., 2018, *ApJ*, 855, L11
- Owen J. E., 2019, *Annu. Rev. Earth Planet. Sci.*, 47, 67
- Parviainen H., 2015, *MNRAS*, 450, 3233
- Riley A., 2017, STIS Instrument Handbook for Cycle 25, Version 16.0. Space Telescope Science Institute, Baltimore
- Shematovich V. I., Ionov D. E., Lammer H., 2014, *A&A*, 571, A94
- Stefansson G. et al., 2020, *AJ*, preprint (arXiv:2007.12766)

- Tamura M. et al., 2012, in McLean I. S., Ramsay S. K., Takami H., eds, Proc. SPIE Conf. Ser. Vol. 8446, Ground-Based and Airborne Instrumentation for Astronomy IV. SPIE, Bellingham, p. 84461T
- Thao P. C. et al., 2020, *AJ*, 159, 32
- Tian F., France K., Linsky J. L., Mauas P. J. D., Vieytes M. C., 2014, *Earth Planet. Sci. Lett.*, 385, 22
- Tody D., 1986, in Crawford D. L., ed., Proc. SPIE Conf. Ser. Vol. 627, Instrumentation in Astronomy VI. SPIE, Bellingham, p. 733
- Triaud A. H. M. J., 2017, The Rossiter–McLaughlin Effect in Exoplanet Research. Springer-Verlag, Berlin, p. 2
- Virtanen P. et al., 2019, *Nat. Methods*, 17, 261
- Watson A. J., Donahue T. M., Walker J. C. G., 1981, *Icarus*, 48, 150
- Wright N. J., Newton E. R., Williams P. K. G., Drake J. J., Yadav R. K., 2018, *MNRAS*, 479, 2351
- Yasui C. et al., 2019, *ApJ*, 886, 115
- Youngblood A. et al., 2016, *ApJ*, 824, 101

This paper has been typeset from a  $\text{\TeX/L\AA\TeX}$  file prepared by the author.